Effect of calcium on the thermal denaturation of whey proteins and subsequent fouling in a benchtop fouling device: An experimental and numerical approach

Weiji Liu, Yuting Feng, Fei Pan, Romain Jeantet, Christophe André, Xiao Dong Chen, Guillaume Delaplace

Available online at www.sciencedirect.com

Food and Bioproducts Processing

journal homepage: www.elsevier.com/locate/fbp

Effect of calcium on the thermal denaturation of whey proteins and subsequent fouling in a benchtop fouling device: An experimental and numerical approach

Weiji Liu[a,b,e,*], Yuting Feng[a], Fei Pan[a], Romain Jeantet[c,e], Christophe André[d], Xiao Dong Chen[a,e], Guillaume Delaplace[b,e,**]

[a] School of Chemical and Environmental Engineering, Soochow University, Suzhou, Jiangsu 215123, PR China
[b] University of Lille, CNRS, INRAE, Centrale Lille, UMR 8207 - UMET - Unité Matériaux et Transformations, F-59000 Lille, France
[c] STLO, INRAE, Institut Agro, 35042, Rennes, France
[d] Junia Hei, 13, rue de Toul, BP 41290, 59014 Lille Cedex, France
[e] International Joint Laboratory (INRAE Villeneuve d'Ascq-Soochow University-Agrocampus Rennes), School of Chemical and Environmental Engineering, College of Chemistry, Chemical Engineering and Materials Science, Soochow University, Suzhou, Jiangsu 215123 PR China

ARTICLE INFO

Article history:
Received 4 May 2022
Received in revised form
7 September 2022
Accepted 8 September 2022
Available online 13 September 2022

Keywords:
Whey protein fouling
Ionic calcium
Benchtop fouling device
3D CFD simulation
Temperature quantification
Pyrromethene 556

ABSTRACT

The key role of calcium in whey protein fouling behavior is well known in plate heat exchangers (PHEs), as it affects both the thermal denaturation of proteins and deposition reaction on the surface. However, the complex flow pattern and the closed configuration of PHEs make it hard to investigate this phenomenon *in situ*. In this paper, a microchannel benchtop fouling device was designed, making it possible to achieve a similar temperature profile to that performed in PHEs but in a laminar regime. A 3D simulation was developed to predict the thermal denaturation of β-lactoglobulin (BLG) as well as its deposition in the microchannel using computational fluid dynamics (CFD). The thermodynamics and heat transfer of the numerical model was validated by experimentally measuring the bulk fluid temperature profile in the microchannel using fluorescence microscopy, where Pyrromethene 556 was used as a temperature indicator. Results revealed a quasi-linear relationship between the pre-exponential factor of deposition reaction and the calcium concentration, implying that the fouling was built in such a pattern that only one calcium ion per one BLG molecule is involved. The imaging of the fouling deposit *in situ* showed spherical structures of deposits at low calcium levels, while denser and more rod-like ones were found at higher calcium concentrations. The fouling behavior was found to follow a crystallization-like pattern with preference upon the previously fouled layer instead of clean stainless steel surface. These findings confirm the essential role of ionic calcium on the formation of fouling deposits by anchoring the denatured BLG protein upon the surface as well as strengthening the protein-protein interactions for fouling build-up.

* Corresponding author at: School of Chemical and Environmental Engineering, Soochow University, Suzhou, Jiangsu 215123, PR China.
** Corresponding author at: University of Lille, CNRS, INRAE, Centrale Lille, UMR 8207 - UMET - Unité Matériaux et Transformations, F-59000 Lille, France.
E-mail addresses: liu.weiji@inrae.fr (W. Liu), guillaume.delaplace@inrae.fr (G. Delaplace).
https://doi.org/10.1016/j.fbp.2022.09.002
0960-3085/

Nomenclature

Symbols

A	Emitted light collection fraction.
C_i	Concentration of species i ($kg \cdot m^{-3}$).
C_{S0}	Inlet BLG concentration ($kg \cdot m^{-3}$).
C_p	Specific heat capacity ($J \cdot kg^{-1} \cdot K^{-1}$).
d_i	Particle diameter of species i (m).
D_i	Diffusion coefficient of species i ($m^2 \cdot s^{-1}$).
[Dye]	Concentration of the dye ($mol \cdot m^{-3}$).
Ea	Activation energy ($J \cdot mol^{-1}$).
F	Volume force vector ($N \cdot m^{-3}$).
I	Unit vector.
I_0	Excitation light intensity.
k	Thermal conductivity ($W \cdot m^{-1} \cdot K^{-1}$).
k_i	Reaction rate constant ($mol^{-1} \cdot m^3 \cdot s^{-1}$).
k_{0i}	Pre-exponential factor of reaction i ($mol^{-1} \cdot m^3 \cdot s^{-1}$).
$\mathbf{N}_i$	Mass flux of species i ($kg \cdot m^{-2} \cdot s^{-1}$).
N_{AV}	Avogadro constant ($6.023 \cdot 10^{23}$ mol^{-1}).
p	Pressure (Pa).
Q	Heat sources ($W \cdot m^{-3}$).
q	Heat flux ($W \cdot m^{-2}$).
R	Universal gas constant ($8.314\,J \cdot mol^{-1} \cdot K^{-1}$).
T	Temperature (K).
T_{in}	Inlet fluid temperature (K).
u	Velocity vector ($m \cdot s^{-1}$).
v_{in}	Inlet fluid velocity ($m \cdot s^{-1}$).
V_i	Molar volume of the particles i ($mol \cdot m^{-3}$).
ΔH	Enthalpy of activation ($J \cdot mol^{-1}$).
ΔS	Entropy of activation ($J \cdot mol^{-1}$).

Greek letters

α	Unfolding ratio.
δ	Sample thickness (m).
δ_0	Thickness of microchannel (3.5 mm).
ε	Extinction coefficient of the dye ($m^2 \cdot mol^{-1}$).
μ	Fluid viscosity (Pa·s).
ρ	Density ($kg \cdot m^{-3}$).
Φ	Quantum yield of the dye.

Subscript

agg	Aggregated BLG.
Al	Aluminum.
D	Deposition process.
N	Native BLG.
S	Soluble BLG.
U	Unfolded BLG.

1. Introduction

The unwanted formation of deposits upon the hot surface of the stainless steel in the plate heat exchanger (PHE) during thermal processing is an unresolved problem in the dairy industry. These fouled layers reduce heat transfer efficiency, therefore deteriorating the quality of the product (Fryer et al., 2006). Operating costs are further increased by frequent shutdowns for cleaning and the corresponding use of cleaning detergents (Georgiadis et al., 1998b; Gillham et al., 1999). After decades of study, it has long been recognized that the thermal denaturation of the main component of the whey protein (*i.e.*, β-lactoglobulin, BLG) is the key that drives fouling (Anema, 2020; Bansal and Chen, 2006; Sadeghinezhad et al., 2015; Wijayanti et al., 2014). Generally, BLG denaturation can be described using a two-step consecutive reaction as N→U→A where the native BLG (N) unfolds its tertiary structure and expose a free thiol group. The unfolded BLG (U) becomes activated and can interact with other denatured whey proteins or with κ-casein on the casein micelle surface to form aggregates (A) through thiol/disulfide exchange reactions (Creamer et al., 2004; Sawyer, 1969; Shimada and Cheftel, 2002; Vasbinder and de Kruif, 2003; Verheul et al., 1998).

It is widely accepted that the unfolded BLG generated in the bulk is the precursor for fouling growth. This hypothesis has been proven in many studies, for example, Bouvier et al. (2014) found a very strong correlation between the unfolded BLG concentrations and the amount of fouling deposits inside a pilot plant PHE. Besides that, only the Raman signatures of unfolded BLG were identified inside the whey protein fouling deposits, implying an essential role of unfolded BLG on the fouling growth (Blanpain-Avet et al., 2012). For this and other reasons, the thermal denaturation kinetics of BLG has been extensively studied (Anema and McKenna, 1996; Dannenberg and Kessler, 1988; Oldfield et al., 1998). In fact, other milk components such as caseins or calcium ions can significantly affect the denaturation of BLG thus affecting the overall fouling behavior (Anema and Li, 2003; Petit et al., 2011). In particular, calcium ion has been recently noted as a key element in fouling as it has a dramatic impact both on the denaturation of the proteins and the deposition processes (Khaldi et al., 2018). However, most of the attention has been paid on the calcium effect concerning the thermal denaturation of BLG. For instance, ionic calcium was found to have a protective role on the unfolding step of BLG denaturation by showing increased activation energy with elevated calcium concentrations (Petit et al., 2011). On the contrary, an ion-specific interaction between calcium and native BLG was found which induces local unfolding of the protein and exposition of its free thiol group (Jeyarajah and Allen, 1994). Moreover, calcium also takes part in the intramolecular electrostatic shielding of BLG negative charges that lowers the Coulomb repulsion between proteins and favors the aggregation process (Simons et al., 2002). In more recent research, Ca^{2+} was proposed to have a specific binding site on the unfolded BLG molecule, which might be a necessary feature to form protein aggregates (de sa et al., 2019). Despite what has been mentioned above, how calcium affects the fouling reaction kinetics has never been studied exhaustively.

Conceptually, dairy fouling consists of thermal denaturation of proteins in the bulk, mass transfer as well as surface reactions (*i.e.* deposition) (Belmar-Beiny et al., 1993). The first two can be nowadays well calculated in a given geometry by using computational fluid dynamics (CFD) combined with thermal denaturation kinetic models. However, the surface reaction was either empirically estimated using the Biot number (Fryer, 1989) or adsorption rates (De Jong, 1997), the latter being mathematically identical to a surface reaction. From an experimental point of view, it is still a great challenge to perform real-time measurements on the fouling deposition, particularly with similar temperatures and hydrodynamics to industry-like fouling experiments such as those in PHEs. It is rare to see dynamic measurement of fouling mass in PHEs in the literature as it is typically destructive (the plate has to be dismantled and dried), and therefore difficult to determine kinetics. There are only few studies that could provide dynamic measurements on the protein deposition, for example, Kroslak et al. (2007)

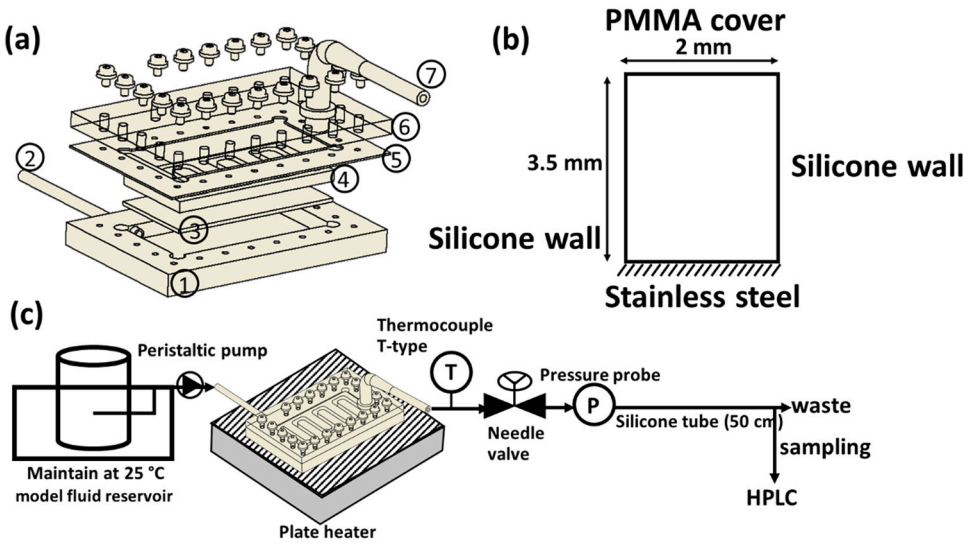

Fig. 1 – (a) 3D schematic of the dismantled benchtop fouling device. The device is assembled with (from bottom to up) aluminum alloy substrate (1), 304 stainless steel tube (2), 316 stainless steel plate (3), silicone tunnel wall (4), silicone rubber (5), PMMA cover (6) and 3D-printed nylon bend tube (7). (b) Dimensions of the rectangular cross-section in the u-shape tunnel. (c) experimental set-up for fouling runs.

studied the deposition kinetics of BLG at a solid-liquid interface with optical lightmode spectroscopy over a range of temperatures between 61 and 83 °C. Santos et al. (2006) studied the adsorption of whey proteins on modified and unmodified 316 2R stainless steel surfaces under well-defined flow conditions using *in situ* ellipsometry. These studies provide direct real-time information of the deposited protein mass, yet they have not been coupled with denaturation/aggregation reactions in the bulk to investigate the surface reactions.

There have been numerous simulation studies based on typical Arrhenius models for milk fouling phenomenon in one-dimensional (1D) (Grijspeerdt et al., 2004; Nema and Datta, 2006; Sahoo et al., 2005), or in two-dimensional environments (2D) (De Bonis and Ruocco, 2009; Jun et al., 2004; Jun and Puri, 2006; Mahdi et al., 2009). These studies generally applied a crude simplification on the surface kinetics by using overall parameters, such as bulk temperature in the channel or unfolded BLG concentration in the bulk. In this case, a three-dimensional (3D) simulation is preferred as it allows to take real geometry and flow conditions into account and therefore provides localized information such as surface temperature, relevant hydrodynamics and unfolded BLG concentration on the surface (Jun and Puri, 2005). However, 3D modeling in PHEs is extremely computationally expensive, and would inevitably incur a cost penalty that must be balanced against the advantage of being able to predict fouling close to reality. Besides that, the determination of deposition kinetics in PHEs could be complicated due to its complex fluid mechanics. For example, the flow regime shows a contrary effect on the fouling mass: the amount of fouling decreases with increased Reynolds number (Re) from 1800 to 7500 in a concentric tube heat exchanger (Belmar-Beiny et al., 1993), while a higher mass of deposit was found at Re of 3200 than that of 2000 or 5000 in PHE (Guérin et al., 2007; Khaldi et al., 2015).

Consequently, a simpler flow regime such as laminar flow could be preferred for investigating deposition kinetics, although these flow conditions are not representative of industrial processing conditions. Therefore, the first step of this work is to design and build a bench-scale fouling device that could provide simple configuration and thus simple fluid mechanics (*i.e.* laminar regime). Model solutions reconstituted from whey protein isolate (WPI) powders were used to perform fouling runs in the fouling device at a fixed thermal profile. Various ionic calcium levels ranging from 40 to 70 ppm were applied in order to investigate the effect of Ca^{2+} on the surface reaction. The second step consisted in performing a realistic 3D simulation on the whey protein denaturation and subsequent deposition based on the geometry of the fouling device. The bulk fluid temperature in the microchannel of the fouling device was quantified using wide-field fluorescence microscopy to validate the numerical model where the fluorescence dye Pyrromethene 556 (PM556) was selected and used as a temperature indicator. Finally, the kinetic constants for the deposition reaction were achieved with the combination of experimental deposition rates.

2. Experimental procedure

2.1. *Benchtop fouling device*

The 3D structure of the dismantled fouling device is shown in Fig. 1(a). This benchtop device consists of (from bottom to up) 6061 aluminum alloy substrate ($68 \times 44 \times 6\ mm^3$), 304 stainless steel (SS) tube (i.d. 2 mm), SS plate ($48 \times 24 \times ;1\ mm^3$), silicone tunnel wall, silicone rubber, PMMA (polymethyl methacrylate) cover and a 3D-printed nylon bend tube. The SS plate was made from 316 L stainless steel and had been subjected to chemical pickling (treated in a mixture of 30 wt% nitric acid and 8 wt% hydrofluoric acid at room temperature for 45 min) (Hagsten et al., 2019). In order to create a u-shape fluid tunnel, the SS plate was put inside the groove of the substrate before filling with silicone mixture (mixing ratio of 1:1, two-component silicone). PMMA was then placed upon the silicone to create a flat surface. The silicone was cast at 75 °C for at least one hour. After that, the PMMA cover was removed, a CO_2 laser was used to cut the silicone and a u-shape tunnel with a rectangular cross-section of

$2 \times 3.5 \times 158\ mm^3$ (width × height × length, Fig. 1(b)) was created. The whole device was well-sealed *via* screws: it has been tested to be pressure-tolerant (up to least 3 bar) and also allows to avoid any leakage and by-pass of the fluid.

2.2. Model fouling fluid

Whey protein isolate (WPI) was purchased from Davisco Foods International Inc. (Le Sueur, MN, USA), with a protein content > 90 wt% as given by the manufacturer, of which ~65 % is β-lactoglobulin (BLG) and ~27 % α-lactalbumin (α-la). WPI powder was reconstituted with MilliQ water to prepare model solutions at a protein concentration of 0.5 wt% to simulate the whey protein content in raw milk (Farrell Jr et al., 2004). This model protein solution has long been utilized as a test fluid for fouling studies in the literature (Belmar-Beiny et al., 1993). However, it is important to be aware that the presence of casein has been found to have a significant effect on whey protein fouling behavior (Liu et al., 2021). Casein introduces additional molecular events such as co-aggregations (*e.g.* forming κ-casein-BLG complexes) and mineral balancing (*i.e.* reducing calcium ions in the serum phase by transferring them into the colloidal phase during heating). Nevertheless, as the aim of this work is to study how calcium modulates whey protein fouling, the presence of casein is not desirable in this case.

To investigate the effect of Ca^{2+} on the deposition of BLG, various Ca^{2+} levels (40, 45, 50, 55, 60, 65 and 70 ppm) were achieved by adding different amounts of $CaCl_2$ stock solutions (Acros Organics, USA) in the model fluids. The ionic and total calcium of the 0.5 wt% WPI solution (without additional Ca^{2+}) was confirmed to be less than 0.1 and 1 ppm using calcium ion-selective electrode (9720BNWP, Thermofisher, USA) and atomic absorption spectrometry (Vista-MPX, Varian, USA), respectively. It has been verified that all supplemented Ca^{2+} (by adding $CaCl_2$) remained in their ionic forms by using the same protocol. The pHs of the fouling fluids were adjusted to 6.6 by adding either concentrated HCl or NaOH if needed.

2.3. Bench-scale fouling runs

Fouling experiments were performed in the bench-scale setup as shown in Fig. 1(c). Model fouling solutions that remained at 25 °C in a watch bath were pumped into the fouling device through a peristaltic pump at a constant flow rate of $2\ ml{\cdot}min^{-1}$. The fouling device was mounted upon a plate heater (TP104SC, Instec, USA) in order to gradually heat up the solution. The surface temperature of the plate heater was set at 90 °C resulting in a temperature profile of the solution ranging from 60° to 83 °C (in the u-shape tunnel). This combination of the flow rate and the surface temperature was selected to have a thermal profile that mimics a high temperature short time (HTST) pasteurization process similar to that previously performed in a pilot plant PHE, but in a laminar regime (see Supplementary information, Fig. S1) (Liu et al., 2021). This was achieved by temperature quantification using fluorescence as described in the later section. A T-type thermocouple (accuracy ± 0.5 °C) was placed at the outlet of the fouling device so as to monitor the experimental temperature of the fluid at the outlet. In order to avoid bubble formation during heating, the whole system was pressurized by providing a back pressure (~1 bar) using a stainless steel needle-type valve. A silicone tube (~ 50 cm) was connected to the outlet of the fouling device which allows a natural cooling and sampling of the solution. Before pumping fouling fluid, Milli Q water was firstly used to reach a thermal equilibrium of the system at the desired process temperature. After that, fouling solutions were processed at different durations, depending on calcium levels. In general, solutions with lower calcium levels required longer times to obtain a significant amount of deposit (≥ 1 mg), while for those with higher Ca concentrations, the processing was shortened to avoid blocking of the channel (*e.g.*, 4 h for 40 ppm Ca^{2+} and 30 min for 65 ppm Ca^{2+}).

During each fouling run, samples were taken at the end of the silicone tube typically three times (at beginning/middle/end). Brightview images (obtained using bright light) were also captured during fouling experiments at different time intervals to dynamically monitor the morphology evolution of fouling deposits in the microchannel. More details of the microcopy system will be described in the later section. When the fouling experiments were finished, water was used again to replace fouling solutions in the channels; the fouling deposit at the end of each fouling run was also imaged. After imaging, the fouling device was dismantled and the SS plate was dried at 50 °C overnight (with removal of the silicone wall). The dried deposit mass was calculated by the difference between bare and fouled plates.

2.4. Determination of soluble BLG concentration using size-exclusive chromatography

The sample solutions collected from each fouling run were allowed to return to room temperature before adjusting the pH of the solutions to 4.6 to precipitate the aggregates. The precipitations were removed by centrifugation at 16,100× *g* at 4 °C for 30 min. The BLG in the supernatant or the soluble BLG was considered to consist of native BLG, as well as those unfolded BLG that refolded back to the native state. This has been confirmed by Delahaije et al. (2016) as they found that the nonaggregated BLG at pH 4.6 presented identical secondary structure to that of native BLG using circular dichroism. The supernatant was filtered *via* a 0.22 µm PVDF filter before injecting 20 µL into the HPLC system (ThermoFisher UltiMate 3000). The soluble BLG concentration was detected using size exclusive chromatography (SEC) through an XBridge BEH 200 Å 3.5 µm column (Waters, USA). A 50 mM phosphate buffer at pH 7.0 and $0.7\ ml{\cdot}min^{-1}$ with UV detection at 280 nm was used. Pure BLG powder (≥90 %) was purchased from a domestic company (Shanghai yuanye Bio-Technology Co., Ltd, China) for calibration purposes.

2.5. Temperature quantification using wide-field fluorescence microscopy

As mentioned in Section 2.3, varying flow rate of the fluid in the microchannel and the bottom surface temperature of the plate heater can result in different temperature profiles of the fluid and therefore different thermal history. It is of great importance to quantify the solution temperature in the channel in order to find suitable operating parameters. Fluorescence-based technique has been found to be a novel non-invasive method for quantitatively mapping solution temperature with high spatial resolution in microfluidic systems (Benninger et al., 2006). Rhodamine B (RhB) is one of the most commonly used dyes for thermometry (Paviolo

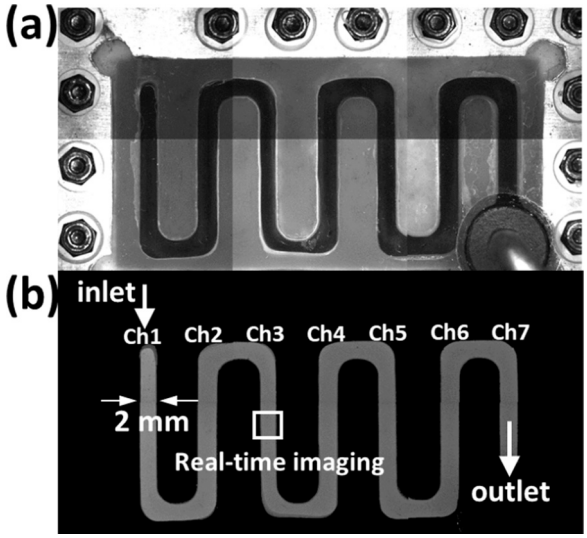

Fig. 2 – (a) Brightview and (b) fluorescence image of the microchannel in the bench-scale fouling device. Each image was processed and merged from six different images. (b) was captured with 10 μM PM556 at a flow rate of 2 ml·min^{-1} and a constant bottom surface temperature at 90 °C. Images were obtained at the lowest magnification, i.e. 7.13 × . Notice that a black-Ti 304 stainless steel was used in the case of fluorescence measurement instead of a normal 316 L SS plate in order to avoid the reflection effect. Channels are named from one to seven starting from the inlet as noted in the image.

et al., 2013), while it was not selected in this paper as RhB is well-known to interact/adsorb with many inorganic or organic materials, including silicone (Smart, 1977). Instead, the fluorescence dye Pyrromethene 556 (PM556) was selected due to its superior photostability without adsorption in the microchannel.

PM556 supplied from Exciton (USA) was used as received. Fluorescent solutions of 10 μM PM556 were prepared by dilution of a concentrated stock solution (in acetone). The calibration curve was obtained by placing the solutions into a 1 mm thick glass cuvette with a T-type thermocouple to monitor the solution temperature. The cuvette was well-sealed to avoid evaporation of the solvent (*i.e.*, water). The cuvette was put upon the plate heater at desired temperatures ranging from 25° to 90 °C; once the thermal steady state was reached, fluorescence measurements were performed using a conventional wide-field microscope (WFM) as reported previously (Liu et al., 2017). In short, the WFM consists of a wide-field fluorescence microscope (MacroZoom Z16, Leica) and a × 1.0 planapochromatic objective (magnification 7.13 ×–115 ×). PM556 was excited at a wavelength of 470 nm (25 nm bandwidth, LED4D067, Thorlabs), and its fluorescence emission was recorded as 8-bit images with a monochrome CCD camera (ICX285ALCCF, ToupTek, 1360 × 1024 pixels). The experiments were replicated at least three times.

In order to quantify the solution temperature in the fouling device, the fluorescent solution of PM556 was used instead of fouling solutions. It was decided to fix the flow rate at 2 ml·min^{-1} (averaged Reynolds number *Re* of 30, mean residence time of ~33 s in the u-shape tunnel) while varying the surface temperature of the plate heater from 60° to 90°C. As it can be seen in Fig. 2(a), typically six images were needed to obtain the whole view of the channel due to the limited field of view (at lowest magnification 7.13 ×). Matlab® was used for image processing, including correction of the uneven illumination, alignment, image merging and thresholding as described in (Liu et al., 2018). The processed image containing only fluorescence information of the channel is shown in Fig. 2(b). A 2D motorized stage (WN268TA50M, Winner Optics, Beijing, China) was coupled with the plate heater so as to move the fouling device for imaging at different positions of the device.

The fluorescence captured in the WFM system is known to be the integration of the intensity along the sample height (z-axis), therefore the fluorescence intensity I_f of PM556 in the microchannel can be described as (no photo-bleaching):

$$I_f = I_0 A \Phi \varepsilon \delta_0 [Dye] \quad (1)$$

where I_0 is the excitation light intensity, A is the emitted light collection fraction, Φ is the quantum yield of the dye, ε ($m^2 \cdot mol^{-1}$) is extinction coefficient of the dye at the excited wavelength, δ_0 (m) is the solution thickness, and [Dye] is the concentration of the dye ($mol \cdot m^{-3}$). If there is a temperature gradient in the z-axis (or quantum yield gradient) as in our case with a heating resource at the bottom surface in a laminar flow scheme, Eq. 1 should be modified as:

$$I_f = I_0 A \Phi' \varepsilon \delta_0 [Dye] \quad (2)$$

The Φ' refers to the mean quantum yield of the dye in the whole solution thickness:

$$\Phi' = \frac{\int_0^{\delta_0} \Phi_\delta d\delta}{\delta_0} \quad (3)$$

where Φ_δ refers to the quantum yield of PM556 at z position δ. In this way, the mean value of solution temperature can be directly calculated using ratiometry by taking 25 °C as the reference. Because of this, the fluorescence of the solution channel in the fouling device at 25 °C with no flow rate was firstly obtained for subsequent temperature calculation. One should notice that a black-Ti 304 SS plate was used instead of 316L SS in fluorescence measurements to avoid reflection effect of the stainless steel on the fluorescence that interrupts the experiments.

For real-time monitoring the fouling deposits, top Brightview images were obtained using a full-color camera (MC170 HD, 5MP pixels, Leica) at the maximum magnification (*i.e.*, 115×). To avoid the interruption of turbidity of the solution at high temperatures and high calcium concentrations, it was decided to fix the observation position at the middle of 3rd channel (Ch3).

2.6. 3D simulation of BLG denaturation and deposition in bench-scale fouling device

In this work, a realistic 3D simulation of the thermal denaturation and deposition of BLG inside the laboratory-scale fouling device was achieved by using COMSOL Multiphysics (COMSOL, version 5.3a). The geometry of the whole fouling set-up including benchtop fouling device and outlet silicone tube were designed using the Autodesk Inventor and eventually imported to COMSOL. A physics-controlled mesh was used to mesh the geometry as shown in Fig. 3: a normal element size of meshing was applied for the solid phase, while a fine mesh was used in the solution domain (channel), resulting in a total of 0.42 million discrete elements. Note that the effect of the formation of fouling layer on the flow regime or energy transfer was not taken into account in the

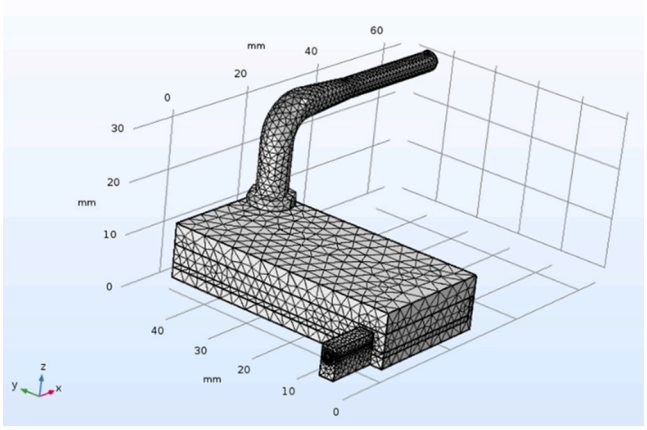

Fig. 3 – Mesh view of the benchtop fouling device. The outlet silicone tube is hidden here to have a better focus on the device. Notice that some parts of the geometry were excluded to minimize the computing time.

simulation as the overall deposition layer was considered to be thin compared to the channel thickness (3.5 mm), so that the solution temperature, protein denaturation and hydrodynamics were not significantly affected due to the formation of fouling deposits (Pan et al., 2019). In other words, the fouling was assumed to follow a linear fouling pattern (*i.e.* constant fouling rate) (Sadeghinezhad et al., 2015).

2.6.1. *The governing equations*

A laminar incompressible flow model based on the Navier-Stokes equation is adopted to describe the fluid flow in the microchannel. The momentum and continuity equations in Cartesian coordinates are respectively:

$$\rho(\boldsymbol{u}\cdot\nabla)\boldsymbol{u} = \nabla\cdot[-p\boldsymbol{I} + \mu(\nabla\boldsymbol{u} + (\nabla\boldsymbol{u})^{T}) + \boldsymbol{F} \quad (4)$$

$$\nabla\cdot(\rho\boldsymbol{u}) = 0 \quad (5)$$

where ρ is the density of the fluid ($kg\cdot m^{-3}$); $\boldsymbol{u}$ is the velocity vector ($m\cdot s^{-1}$); p is the pressure (Pa); μ denotes the viscosity of the fluid (Pa·s); I is a unit vector; F is the external force vector ($N\cdot m^{-3}$).

The energy transfer takes place in the whole model geometry:

$$\rho C_p\boldsymbol{u}\cdot\nabla T + \nabla\boldsymbol{q} = \boldsymbol{Q} \quad (6)$$

where $\mathbf{q}$ is the heat flux ($W\cdot m^{-2}$):

$$\boldsymbol{q} = -k\nabla T \quad (7)$$

And C_p is the specific heat capacity ($J\cdot kg^{-1}\cdot K^{-1}$); T represents the temperature (K), $\mathbf{Q}$ denotes heat sources ($W\cdot m^{-3}$); k is the thermal conductivity ($W\cdot m^{-1}\cdot K^{-1}$), $\boldsymbol{u}$ is $0\ m\cdot s^{-1}$ in the solid domain.

2.6.2. *Thermal denaturation of BLG in the bulk*

The thermal denaturation and aggregation of BLG in the bulk were simulated using the denaturation reaction model as developed by Liu et al. (2022). In this model, it is assumed that the thermal unfolding of BLG occurs instantaneously, and the unfolding of BLG was proposed to be thermodynamically driven following by a kinetically controlled aggregation step:

$$N \rightleftharpoons U \rightarrow A \quad (8)$$

where a chemical equilibrium between native BLG (N) and unfolded BLG (U) is instantaneously established at a given temperature. As the soluble BLG (S) detected using SEC is the sum of native and unfolded BLG (*i.e.*, $C_s = C_N + C_U$), the proportion of the unfolded BLG in the total soluble BLG in the equilibrium, or defined as unfolding ratio α is:

$$C_U = \alpha\cdot C_S \quad (9)$$

The unfolding ratio α can be calculated from the corresponding enthalpy ΔH and entropy ΔS according to van't Hoff's equation:

$$\alpha = 1/\left[1 + \exp\left(\frac{\Delta H}{RT} - \frac{\Delta S}{R}\right)\right] \quad (10)$$

The subsequent reaction of aggregation or polymerization of unfolded BLG species can be expressed as:

$$-\frac{dC_{U,agg}}{dt} = k_{agg}\cdot C_U^2 \quad (11)$$

where k_{agg} is the reaction constant for the aggregation step. The temperature dependence of k_{agg} can be deduced from the Arrhenius equation:

$$k_{agg} = k_{0,agg}\exp\left(\frac{-Ea_{agg}}{RT}\right) \quad (12)$$

where k_{0agg} is the denaturation frequency factor ($mol^{-1}\cdot m^3\cdot s^{-1}$), Ea_{agg} is the activation energy ($J\cdot mol^{-1}$), R is the universal gas constant (*i.e.* $8.314\ J\cdot mol^{-1}\cdot K^{-1}$).

As the loss of soluble BLG is solely due to the formation of aggregates, the following equation holds:

$$\frac{\partial C_S}{\partial t} = \frac{dC_{U,agg}}{dt} = -k_{agg}\cdot\alpha^2\cdot C_s^2 \quad (13)$$

The amount of unfolded BLG can be quantified using Eq. 9, and for the remaining native BLG is:

$$C_N = (1-\alpha)\cdot C_S \quad (14)$$

The details of the thermal denaturation model and the corresponding thermodynamic parameters including enthalpy ΔH and entropy ΔS for unfolding equilibrium, and activation energy Ea_{agg} and logarithmic pre-exponential factor $\ln(k_{0,agg})$ for the aggregation step can be found in (Liu et al., 2022). The values are summarized in Table 1.

The velocity in Eq. 4 is used in the mass conservation equations to characterize the convective mass transfer of all different BLG species in the solution domain:

$$\nabla\cdot(-D_i\nabla C_i) + \boldsymbol{u}\cdot\nabla C_i = R_i \quad (15)$$

$$\boldsymbol{N}_i = -D_i\nabla C_i + \boldsymbol{u}C_i \quad (16)$$

Where D_i and C_i represents respectively diffusion coefficient ($m^2\cdot s^{-1}$) and concentration ($kg\cdot m^{-3}$) for different BLG species

Table 1 – Thermodynamic parameters used for simulation at various Ca^{2+} levels (Liu et al., 2022). Note that these values are used without confirmation of precision.

$[Ca^{2+}]$ (ppm)	Denaturation equilibrium		Aggregation	
	ΔH ($kJ\cdot mol^{-1}$)	ΔS ($J\cdot mol^{-1}$)	Ea_{agg} ($kJ\cdot mol^{-1}$)	$\ln(k_{0,agg})$ ($mol^{-1}\cdot m^3\cdot s^{-1}$)
0	125.4	366.1	179.3	55.2
40	209.5	599.6	160.8	51.0
50	224.6	641.3	153.7	49.3
60	232.0	660.2	107.1	34.0
70	255.6	728.2	91.0	28.6

i; R_i is a reaction rate expression ($kg{\cdot}m^{-3}{\cdot}s^{-1}$); $\mathbf{N}_i$ is the mass flux ($kg{\cdot}m^{-2}{\cdot}s^{-1}$).

The diffusion coefficients of these different BLG species were estimated from the Wilke-Chang equation:

$$D_i = \frac{1.310 \times 10^{-17}{\cdot}T}{\mu{\cdot}V_i^{0.6}} \quad (17)$$

with V_i is the molar volume of the particles:

$$V_i = N_{AV}\frac{1}{6}\pi d_i^3 \quad (18)$$

where N_{AV} is the Avogadro constant ($6.023{\cdot}10^{23}$ mol^{-1}) and d_i is the particle diameter of different BLG species (m). Note that since the unfolding of BLG is considered to be instantaneous, there is no need to treat native and unfolded molecules separately. Instead, they were considered as a unity (*i.e.*, soluble BLG particle), and their amount was calculated according to the unfolding ratio α (*e.g.*, Eq. 14). The corresponding particle diameters were used as reported in the literature ($9.8{\cdot}10^{-11}$ m for soluble BLG and $9.91{\cdot}10^{-10}$ m for aggregated BLG molecule) (Georgiadis et al., 1998a).

2.6.3. *Fouling reaction models*

In this paper, we consider that the surface reaction only occurred at the bottom surface of the channel (upon stainless steel) with a reaction order of one:

$$\frac{\partial C_D}{\partial t} = k_D C_U \quad (19)$$

The effect of shear stress on deposit removal is considered to be negligible in the laminar regime employed here (Pan et al., 2019). The calculated shear stress ($\sim 5 \times 10^{-3}$ Pa) is almost three orders of magnitude smaller than the critical value required to maintain a clean surface, *ca.* 2.7 Pa, as reported by Fryer and Slater (1987). The temperature dependence of the deposition reaction constant k_D can also be expressed by the Arrhenius equation:

$$k_D = k_{D0}\exp\left(\frac{-Ea_D}{RT}\right) \quad (20)$$

where k_{D0} is the deposition frequency factor ($m{\cdot}s^{-1}$) and Ea_D is the activation energy ($J{\cdot}mol^{-1}$) for the deposition.

The surface reaction directly determines the deposit flux across the liquid-solid interface. This can be implemented by specifying an outward flux of unfolded BLG on the interface. As described previously, the key objective of this paper is to determine surface reaction kinetics, particularly at various Ca^{2+} levels. The deposition kinetic constant k_D can be calculated by combining the simulated unfolded BLG concentration on the surface C_U with the experimental deposition rates (average value for the whole deposition area). By fixing 45.1 $kJ{\cdot}mol^{-1}$ for the value of the activation energy Ea_D for the deposition process as propossed by (De Jong, 1996), the deposition pre-exponential factor k_{D0} can be calculated at different ionic calcium concentrations.

2.6.4. *Boundary and initial conditions*

The parameters of boundary and initial conditions for the simulation were chosen from experimental conditions in order to provide a more realistic 3D simulation. In the solution domain, the solution with an initial soluble BLG concentration, C_{S0}, flows from the inlet of the device (SS tube) to the outlet (silicone tube) at a fixed velocity of v_{in} and an initial temperature T_{in}. The outlet gauge pressure is set to be 0 Pa. Non-slip conditions are applied for all the walls contacted in the flow channel. Heat transfer takes place in all the simulation domains, and a constant temperature is specific on the bottom surface (aluminum substract) to simulate the heat resource from the plate heater. The bottom surface temperature was measured at 87.5 °C using an infrared thermal imager (Testo 869, Testo, Germany) when set at 90 °C. The heat loss of the fouling device as well as the outlet silicone tube due to the air was achieved by applying an external natural heat convention with an air temperature of 25 °C. The corresponding parameters for boundary and initial conditions are listed in Table 2. The addition of this low concentration of whey proteins or calcium was considered not to significantly affect the physical properties of water; thus the corresponding properties of water were used for the fouling fluid (Petit et al., 2013). The physical properties of the solid phase are shown in Table 3.

Table 2 – Simulation parameters for boundary and initial conditions.

Variables	Values	Units
Initial solid temperature	25	°C
Inlet fluid temperature, T_{in}	25	°C
Inlet fluid velocity, v_{in}	0.0106	$m{\cdot}s^{-1}$
Inlet soluble BLG concentration, C_{S0}	3	$kg{\cdot}m^{-3}$
Inlet aggregated BLG concentration	1×10^{-20}	$kg{\cdot}m^{-3}$
Bottom surface temperature	87.5*	°C
Air temperature	25	°C

*Value experimentally measured using an infrared thermal imager.

In the present work, the hydrodynamics and the heat transfer of the simulation were firstly validated by temperature quantification of the fluid in the channel using fluorescence. Next, the soluble BLG concentration detected using SEC at the outlet of the system was used to confirm the reliability of the denaturation model of BLG in the bulk. Finally, the reaction constant k_D was calculated by coupling the localized concentration of the unfolded BLG C_U with experimental fouling rates. The simulation was performed in a steady-state scenario. Matlab® scripts were developed to couple COMSOL for extracting calculated parameters, such as velocity, temperature, different BLG species concentrations as well as calculation of deposition reaction constant k_D.

3. Results and discussions

3.1. *Hydrodynamics and temperature profiles of the fluid inside fouling device*

The 3D CFD simulation allows to provide comprehensive information regarding the spatial distribution of the fluid velocity and temperature in the microchannel. For example, as shown in Fig. 4(a), a steady laminar flow is developed in the microchannel, with different magnitudes of velocity in the stainless steel (SS) tube and u-shape tunnel sections. This is due to a change in the tunnel geometry from a round pipe to a rectangular duct. Meanwhile, the fluid is heated gradually as it flows along the channel, from 25 °C at the inlet

Table 3 – Physical properties of the solid materials.

Materials	Variables	Value	Units
Aluminum substrate	Specific heat, $C_{p,Al}$	896	$J{\cdot}kg^{-1}{\cdot}K^{-1}$
	Density, ρ_{Al}	2700	$kg{\cdot}m^{-3}$
	Thermal conductivity, k_{Al}	154	$W{\cdot}m^{-1}{\cdot}K^{-1}$
Stainless steel (SS)	Specific heat, $C_{p,SS}$	502.48	$J{\cdot}kg^{-1}{\cdot}K^{-1}$
	Density, ρ_{SS}	8030	$kg{\cdot}m^{-3}$
	Thermal conductivity, k_{SS}	16.27	$W{\cdot}m^{-1}{\cdot}K^{-1}$
PMMA	Specific heat, $C_{p,PMMA}$	1420	$J{\cdot}kg^{-1}{\cdot}K^{-1}$
	Density, ρ_{PMMA}	1190	$kg{\cdot}m^{-3}$
	Thermal conductivity, k_{PMMA}	0.19	$W{\cdot}m^{-1}{\cdot}K^{-1}$
Nylon	Specific heat, $C_{p,Nylon}$	1700	$J{\cdot}kg^{-1}{\cdot}K^{-1}$
	Density, ρ_{Nylon}	1150	$kg{\cdot}m^{-3}$
	Thermal conductivity, k_{Nylon}	0.26	$W{\cdot}m^{-1}{\cdot}K^{-1}$

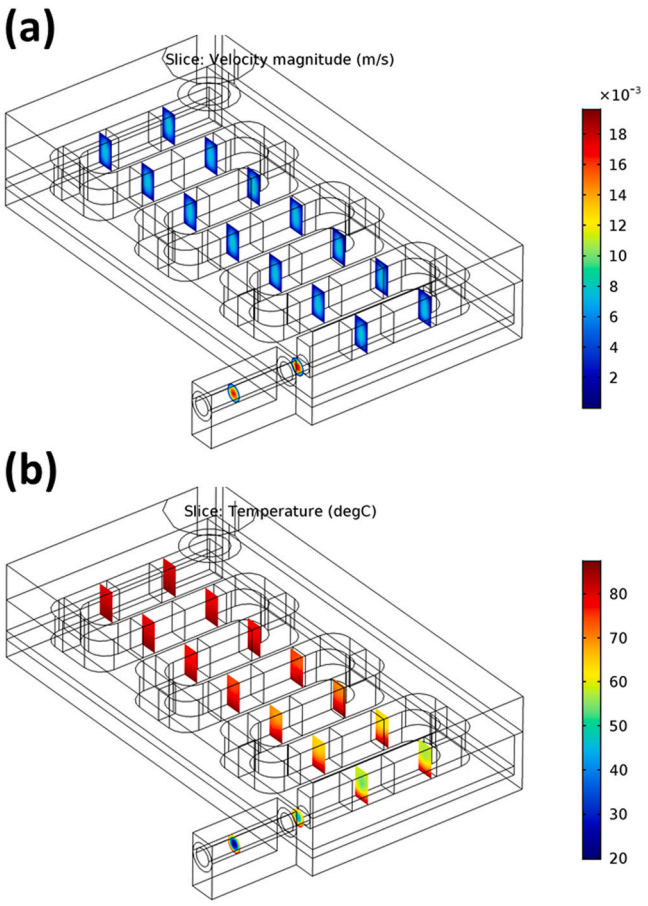

Fig. 4 – Simulated (a) velocity and (b) temperature of the fluid inside the microchannel of the fouling device. Results for the subsequential bend tube and silicone tube are not presented in order to give clear view of the microchannel. The simulation was performed using the boundary conditions in Table 2.

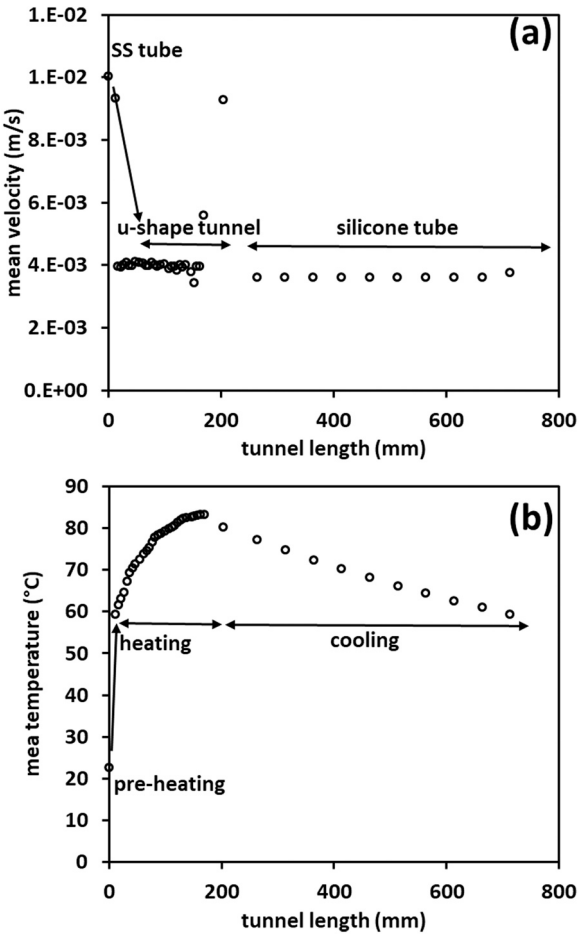

Fig. 5 – Longitudinal mean values of the simulated fluid (a) velocity and (b) temperature along the tunnel length. Results for all sections of the microchannel, including the stainless steel tube, u-shape channel and silicone tube are presented here for overall comparison. Simulation was performed using the boundary conditions in Table 2.

of the SS tube to around 83 °C at the outlet of the u-shape tunnel (Fig. 4(b)).

An overview of how fluid velocity and temperature evolve along the whole microchannel sections, including stainless steel tube, u-shape tunnel and silicone tube is presented in Fig. 5. The mean fluid velocity quickly drops from around 0.01 $m{\cdot}s^{-1}$ to ~4×10^{-3} $m{\cdot}s^{-1}$ when crossing from SS tube to the rectangular duct due to an expanded cross-section (Fig. 5(a)). More importantly, as the SS tube is embedded inside the aluminum substrate, the large heat transfer coefficient in this region allows to quickly heat the solution from 25 °C to around 60 °C (Fig. 5(b)). It can be remarked that this section works as a "pre-heating" zone like those encountered in pilot process lines. The subsequential u-shape tunnel section was noted as a heating zone and is considered to be the main domain where thermal denaturation and deposition of the proteins occur. Finally, the silicone tube acts as a cooling section since the solution temperature gradually decreases to ~60 °C at the outlet. With this outlet

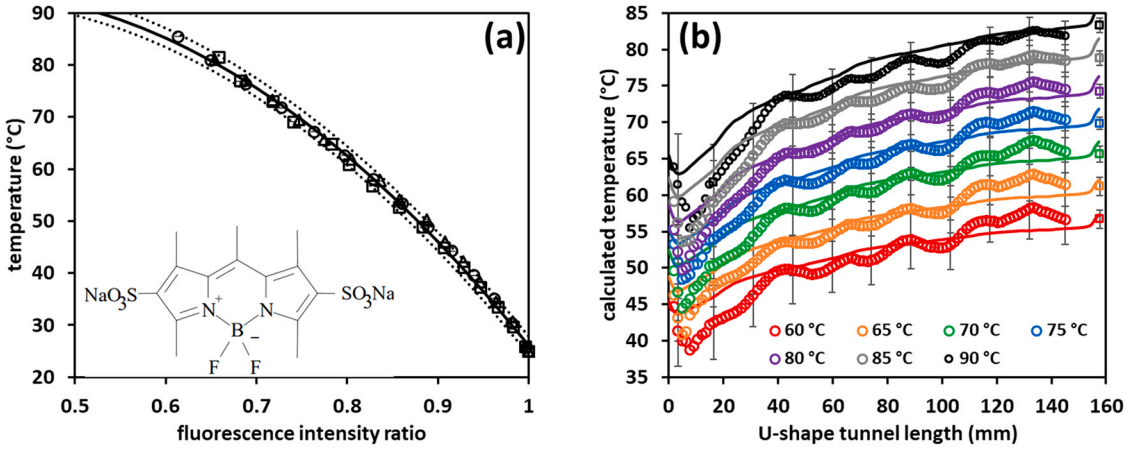

Fig. 6 – (a) Relationship between solution temperature and fluorescence intensity ratio of 10 μM PM556. The fluorescence is normalized at those obtained at 25 °C. Triplicate experiments are displayed. Solid line represents polynomial fitting of the data, dashed lines denote 95 % CI (Confident interval, ± 1.8 °C). Inset shows the molecular structure of PM556. The calculated mean solution temperatures inside the u-shape tunnel using fluorescence are shown in (b). Solid lines represent CFD simulation results. Symbols in square in (b) denote the outlet solution temperature measured using thermocouples. Error bars represent standard deviations (SD) from three individual experiments. Note that the tunnel length in (b) starts from the outlet of the SS tube.

temperature, thermal denaturation of BLG was considered to be stopped.

3.2. *Validation of solution temperature using fluorescence*

As mentioned previously, in order to find proper operating parameters for the fouling run as well as to validate the simulated results, the solution temperature inside the microchannel was quantified using fluorescence ratiometry where PM556 was applied as the temperature indicator. The temperature dependence of 10 μM PM556 solution at various temperatures, normalized by the fluorescence observed at reference temperature 25 °C, is shown in Fig. 6(a). It is clear that at higher temperatures, the fluorescence intensity or the quantum yield of the dye decreases, up to 50 % loss at 90 °C compared to the reference. The decreased quantum yield of the dye at high temperature is generally due to an increase in the non-radiative deactivation process (López Arbeloa et al., 1999). For example, for the dye Rhodamine B, lower solvent viscosity at higher temperatures favors the intramolecular rotational motion of the two dialkylamino groups, leading to a non-emissive TICT-like (Twisted Intramolecular Charge-Transfer) state.

The calibration curve shown in Fig. 6(a) was subsequently applied to map the fluid temperature in the microchannel of the device. The fluorescence profiles generally show decreasing trends along the tunnel with higher fluorescence intensities at lower surface temperatures (Fig. S2). The corresponding mean temperatures of the fluid in the microchannel calculated using fluorescence are shown in Fig. 6(b). Results show that the solution temperature drops suddenly right after exiting the SS tube (or entering the u-shape tunnel) and then increases to a plateau when it reaches the outlet (entering nylon tube). This temperature drop could be due to heat loss on contact with the "cold" silicone wall and the PMMA cover of the channel. This behavior is also recognized by the CFD simulation as shown in solid lines in Fig. 6(b). In general, the temperature profiles calculated using fluorescence match well with simulated ones as well as those outlet temperatures measured using thermocouples (Fig. 6(b)).

3.3. *Thermal denaturation and deposition of BLG in the fouling device*

The heat-induced denaturation and aggregation of BLG in the bulk were achieved using the denaturation model as described previously in Section 2.6.2. Fig. 7(a) shows the simulated native BLG profiles in the microchannel with a 0.5 wt% WPI model solution containing 40 ppm Ca^{2+}. More detailed information of bulk reaction can be seen in Fig. 7(b) by presenting mean concentration profiles of all three different BLG species, including native, unfolded and aggregated ones. The simulated BLG profiles obtained at other calcium concentrations are presented in the Supplementary information (Fig. S3). It can be concluded that the thermal denaturation of BLG mainly occurs in the u-shape tunnel section (*i.e.* heating section) and can be considered negligible in the cooling section as there is little formation of aggregated BLG. The native BLG concentration (C_N) keeps decreasing in the u-shape tunnel reaching a minimum value of ~0.5 g·L^{-1} at the outlet of the nylon tube (~200 mm), while it gradually recovers and reaches ~2 g·L^{-1} at the outlet of the silicone tube due to cooling. This value is almost equal to the soluble BLG concentration (C_S) at the same position, indicating that the native⇌unfolded equilibrium of BLG almost shifts back to the native state at such low temperature condition. Results also confirm a more significant impact of calcium on the aggregation compared to unfolding of BLG as the concentration of the aggregated BLG species are higher with elevated calcium concentrations whilst for the unfolded BLG, it differs little with increased calcium levels (Fig. S3).

To further validate the reliability of the thermal denaturation model, the simulated soluble BLG concentrations at the outlet of silicone tube were compared with experimental results as shown in Fig. 8(a). It is evident that with higher calcium levels, the denaturation level of BLG increases in benchtop fouling system, with little differences at calcium concentrations between 60 and 70 ppm. Additionally, the

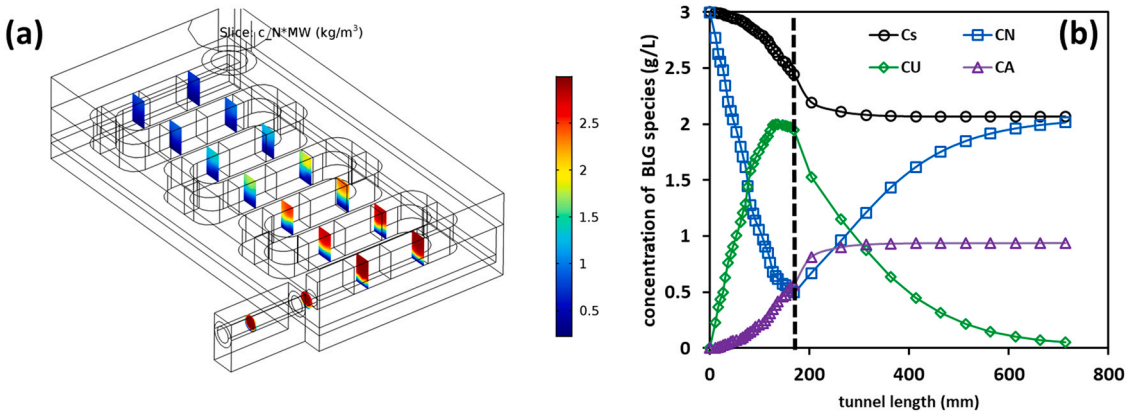

Fig. 7 – (a) 3D CFD simulated native BLG concentrations inside the microchannel. Model fluid contains 0.5 wt% WPI with the addition of 40 ppm Ca^{2+}. (b) Average values of simulated BLG species concentrations along the tunnel length. Vertical dashed line represents the location of the u-shape tunnel outlet (~167 mm). Three different BLG species are shown, including native (C_N), unfolded (C_U) and aggregated ones (C_A). The soluble BLG (C_S) is the sum of native and unfolded BLG species. Solid lines are used to guide the eyes.

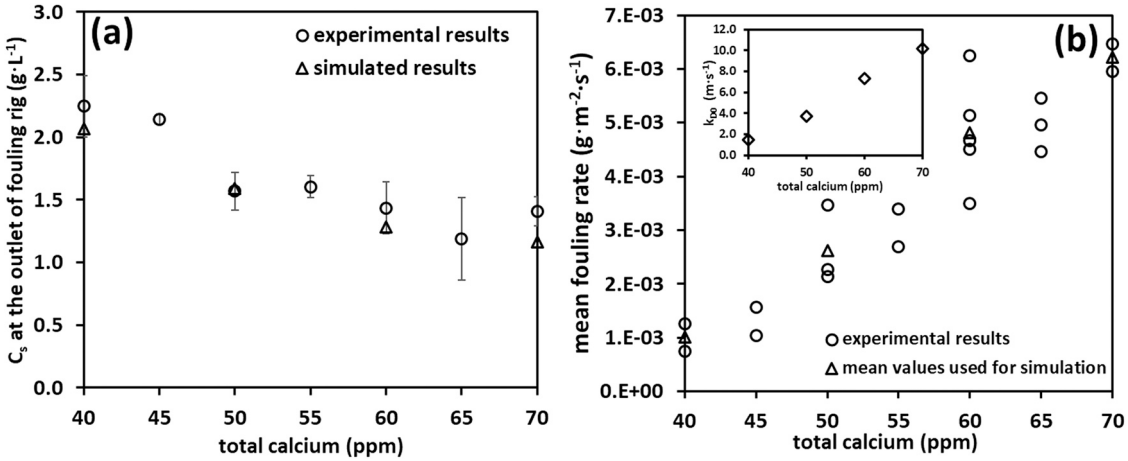

Fig. 8 – (a) Soluble BLG concentrations obtained at the outlet of fouling system (outlet of silicone tube). Symbols in circle represent experimental data while the ones in triangle denote simulated results. Error bars show SD of at least two replicates. (b) Mean fouling rate at various calcium levels. The triangle symbols show average values at specific calcium level which was used for simulation. Inset figure shows the values of k_{D0} for deposition simulation.

simulated results agree well with the experimental data which again, strengthen the validity of our simulation approach. Fig. 8(b) shows a quasi-linear relationship of fouling rate at elevated ionic calcium concentrations. The fouling rates measured here are almost two orders of magnitude higher than those reported in small scale studies with mostly pure BLG without adding calcium (*e.g.* ~0.027 $mg{\cdot}m^{-2}{\cdot}s^{-1}$ at 85 °C) (Santos et al., 2006), or with WPI and addition of calcium but at lower temperatures using QCM (Quartz Crystal Microbalance, ~0.042 $mg{\cdot}m^{-2}{\cdot}s^{-1}$ at 65 °C with 40 ppm Ca^{2+}) (Yang et al., 2018). Nevertheless, our results are more comparable to those performed in large scale fouling experiments in real heat exchangers in pilot plant. For example, our recent study with 0.5 wt% WPI at an ionic calcium of 38.7 ppm report an overall dry deposits of 17.1 g in a 10-passes PHE (temperature ranges from 65° to 85 °C), resulting in mean fouling rates of ~1.6 $mg{\cdot}m^{-2}{\cdot}s^{-1}$) (Liu et al., 2021).

It is important to note that the calculation of surface reaction kinetics needs the localized information of unfolded BLG species (C_U) (Eq. 19). However, the corresponding thermodynamic parameters (for calculating C_U) are only available at four specific calcium concentrations (*i.e.*, 40, 50, 60 and 70 ppm, Table 1). Therefore, only the fouling rates obtained at these four calcium concentrations were used to calculate the corresponding pre-exponential factor for deposition k_{D0} in simulation as listed in Table 4. The dependence of k_{D0} against various calcium concentrations is plotted in the inset of Fig. 8(b). A quasi-linear dependence of k_{D0} on the calcium content was found, implying that the deposition rate of unfolded BLG is proportional to the calcium concentrations (reaction order of one). These results might suggest that only one calcium ion per BLG molecule is involved in the deposition reaction otherwise such evolution with an increase of calcium cannot be observed.

Table 4 – Simulated values of k_{D0} at various calcium levels (Eq. 20).

$[Ca^{2+}]$ (ppm)	40	50	60	70
k_{D0} ($m{\cdot}s^{-1}$)	1.48	3.71	7.33	10.17

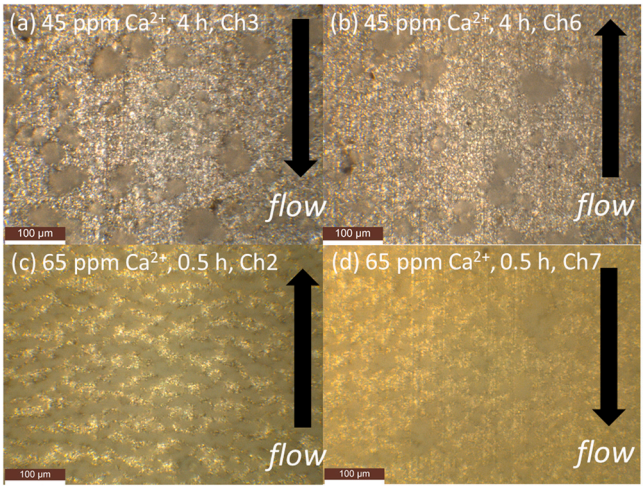

Fig. 9 – Fouling images in the microchannel of 0.5 wt% WPI with the addition of 45 ppm Ca^{2+} obtained at (a) 3rd channel Ch3 and (b) 6th channel Ch6 after 4 h fouling runs, or with the addition of 65 ppm Ca^{2+} observed at (c) 2nd channel Ch2 and (d) 7th channel Ch7 after 30 min fouling runs. Arrows in the images represent the flow direction. The yellowish images in (c) and (d) are due to the formation of fouling deposits on the surface of PMMA cover. Images were all taken at the maximum magnification (*i.e.*, 115×).

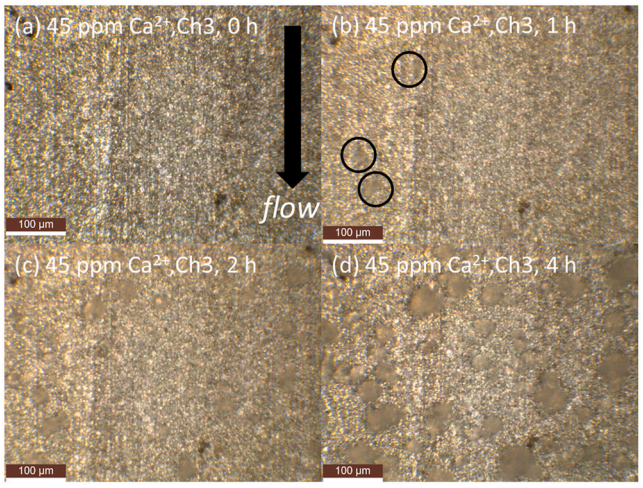

Fig. 10 – Fouling images in the 3rd microchannel (Ch3) of 0.5 wt% WPI with the addition of 45 ppm Ca^{2+} obtained at different fouling times: (a) 0 h, (b) 1 h, (c) 2 h and (d) 4 h. Arrow in (a) represents the flow direction. Apparent fouling deposits can be observed after 1 h fouling run as circled in (b). Images were all taken at the maximum magnification (*i.e.*, 115×).

There is a key difference of the heat transfer between our fouling device system and a usual PHE. In PHEs, the temperature of the fouling fluid is increased by transferring the heat from the hot medium (usually hot water) through the plate, thus both the bulk and surface temperature in the channel are gradually increased. However, in our benchtop fouling device system, the solution temperature in the bulk also increased along the tunnel, but the surface temperature remained almost unchanged (Fig. S4). In this scenario, the surface reaction rates were expected to be almost constant in the tunnel (as poorly affected by surfaced temperature increase along the tunnel) even slightly decreased along the tunnel due to lower content of unfolded BLG concentration as can be seen in the simulated deposition rate profiles (Fig. S5). Therefore, if we consider the fouling mainly limited on the surface reaction, the fouling growth is unlikely to be dependent on the locations in the microchannel.

Our experimental results support this idea as the amount of deposits observed downstream is slightly lower than observed upstream of the microchannel as shown in Fig. 9. At low calcium concentration, the fouling deposits are more spherical with up to ~50 μm in diameter (Fig. 9(a) and (b)). In contrast, deposits are denser and grow to a more rod-like structure perpendicular to the flow direction at high concentrations of calcium (Fig. 9(c) and (d)). These morphologies of the fouling deposit suggest a limited effect of the flow on the formation of deposition as expected for a laminar flow scheme. The dynamic imaging of the channel revealed a crystallization-like fouling behavior as shown in Fig. 10. At low calcium concentrations such as 45 ppm, almost one hour was needed to visualize fouling deposits (Fig. 10(b)). After that, fouling kept growing based on the previously fouled layer. This finding suggests that the unfolded BLG species are preferred to interact with fouled layer for fouling growth instead of deposition upon the clean stainless steel surface. This behavior could also be seen at high calcium concentrations, however, the apparent fouling was denser in this case, and was found within 20 min at a calcium concentration of 60 ppm (Fig. S6). All these results confirm an essential role of Ca^{2+} that it not only helps the anchoring of proteins upon the stainless steel surface but also facilitates the depositing by strengthening the protein-protein cross-linking.

4. Conclusions

In this work, a bench-scale fouling device was successfully built to perform whey protein fouling at various ionic calcium concentrations in a laminar regime. This flow scheme avoids the complicated fluid mechanics induced by turbulent flow, and generates wall shear stresses which are not expected to promote deposit removal. Thanks to the simplicity of the configuration, a realistic 3D CFD simulation was achieved to couple the thermal denaturation and aggregation of BLG in the channel (bulk reaction) as well as its deposition (surface reaction). To validate the simulation model, fluorescence was firstly used to spatially quantify the solution temperature in the channel where PM556 was applied as the temperature indicator. The soluble BLG concentrations detected using HPLC at the outlet of the system satisfactorily matched the simulated values, strengthening the reliability of the numerical model. With the ability to provide reliable information of the localized unfolded BLG concentrations, the deposition kinetics were calculated coupling with experimental fouling rates. The simulation revealed a linear relationship between the pre-exponential factor for the deposition (k_{D0}) and calcium, suggesting that fouling grows in a pattern such that for each unfolded BLG molecule deposited, one calcium ion is involved. The real-time imaging in the channel made it possible to visualize the fouling growth, showing a crystallization-like pattern. The formation of the fouling showed a preference for the previously fouled layer over the clean stainless steel surface. Furthermore, our results confirmed that ionic calcium is essential to fouling

growth with significant effects both on thermal denaturation and deposition processes. This custom-built bench-scale fouling device, although presents some limitations (laminar regime), shows valuable advantages compared to PHEs as it is both energy and material saving with the capacity of real-time optical measurement.

Declaration of Competing Interest

The authors declare that they have no known competing financial interests or personal relationships that could have appeared to influence the work reported in this paper.

Acknowledgments

This work was supported by project funding from the National Key Research and Development Program of China (International S&T Cooperation Program, ISTCP, Project No. 2016YFE0101200). It was also supported by International Join Laboratory collaborative project FOODPRINT between INRAE, Agrocampus and Soochow University. The authors acknowledge Prof. Jie Xiao from Soochow University for providing the computational resources.

Appendix A. Supporting information

Supplementary data associated with this article can be found in the online version at doi:10.1016/j.fbp.2022.09.002.

References

Anema, S.G., 2020. Chapter 9 - The whey proteins in milk: thermal denaturation, physical interactions, and effects on the functional properties of milk. In: Boland, M., Singh, H. (Eds.), Milk Proteins, third ed. Academic Press, pp. 325–384.

Anema, S.G., Li, Y., 2003. Association of denatured whey proteins with casein micelles in heated reconstituted skim milk and its effect on casein micelle size. J. Dairy Res. 70, 73–83.

Anema, S.G., McKenna, A.B., 1996. Reaction kinetics of thermal denaturation of whey proteins in heated reconstituted whole milk. J. Agric. Food Chem. 44, 422–428.

Bansal, B., Chen, X.D., 2006. A critical review of milk fouling in heat exchangers. Compr. Rev. Food Sci. Food Saf. 5, 27–33.

Belmar-Beiny, M.T., Gotham, S.M., Paterson, W.R., Fryer, P.J., Pritchard, A.M., 1993. The effect of Reynolds number and fluid temperature in whey protein fouling. J. Food Eng. 19, 119–139.

Benninger, R.K., Koç, Y., Hofmann, O., Requejoisidro, J., Neil, M.A., French, P.M., Demello, A.J., 2006. Quantitative 3D mapping of fluidic temperatures within microchannel networks using fluorescence lifetime imaging. Anal. Chem. 78, 2272–2278.

Blanpain-Avet, P., Hédoux, A., Guinet, Y., Paccou, L., Petit, J., Six, T., Delaplace, G., 2012. Analysis by Raman spectroscopy of the conformational structure of whey proteins constituting fouling deposits during the processing in a heat exchanger. J. Food Eng. 110, 86–94.

Bouvier, L., Moreau, A., Ronse, G., Six, T., Petit, J., Delaplace, G., 2014. A CFD model as a tool to simulate β-lactoglobulin heat-induced denaturation and aggregation in a plate heat exchanger. J. Food Eng. 136, 56–63.

Creamer, L.K., Bienvenue, A., Nilsson, H., Paulsson, M., van Wanroij, M., Lowe, E.K., Anema, S.G., Boland, M.J., Jiménez-Flores, R., 2004. Heat-Induced redistribution of disulfide bonds in milk proteins. 1. Bovine β-lactoglobulin. J. Agric. Food Chem. 52, 7660–7668.

Dannenberg, F., Kessler, H.G., 1988. Reaction kinetics of the denaturation of whey proteins in milk. J. Food Sci. 53, 258–263.

De Bonis, M.V., Ruocco, G., 2009. Conjugate fluid flow and kinetics modeling for heat exchanger fouling simulation. Int. J. Therm. Sci. 48, 2006–2012.

De Jong P., 1996. Modelling and optimization of thermal processes in the dairy industry. Delft Univ. of Tech. Delft, The Netherlands.

De Jong, P., 1997. Impact and control of fouling in milk processing. Trends Food Sci. Technol. 8, 401–405.

Delahaije, R.J.B.M., Gruppen, H., van Eijk–van Boxtel, E.L., Cornacchia, L., Wierenga, P.A., 2016. Controlling the ratio between native-like, non-native-like, and aggregated β-lactoglobulin after heat treatment. J. Agric. Food Chem. 64, 4362–4370.

Farrell Jr, H.M., Jimenez-Flores, R., Bleck, G.T., Brown, E.M., Butler, J.E., Creamer, L.K., Hicks, C.L., Hollar, C.M., Ng-Kwai-Hang, K.F., Swaisgood, H.E., 2004. Nomenclature of the proteins of cows' milk – sixth revision. J. Dairy Sci. 87, 1641–1674.

Fryer, P.J., 1989. The uses of fouling models in the design of food process plant. Int. J. Dairy Technol. 42, 23–29.

Fryer, P.J., Slater, N.K.H., 1987. A novel fouling monitor. Chem. Eng. Commun. 57, 139–152.

Fryer, P.J., Christian, G.K., Liu, W., 2006. How hygiene happens: physics and chemistry of cleaning. Int. J. Dairy Technol. 59, 76–84.

Georgiadis, M.C., Rotstein, G.E., Macchietto, S., 1998a. Modelling and simulation of complex plate heat exchanger arrangements under milk fouling. Comput. Chem. Eng. 22, S331–S338.

Georgiadis, M.C., Rotstein, G.E., Macchietto, S., 1998b. Optimal design and operation of heat exchangers under milk fouling. AIChE J. 44, 2099–2111.

Gillham, C.R., Fryer, P.J., Hasting, A.P.M., Wilson, D.I., 1999. Cleaning-in-place of whey protein fouling deposits: mechanisms controlling cleaning. Food Bioprod. Process. 77, 127–136.

Grijspeerdt, K., Mortier, L., De Block, J., Van Renterghem, R., 2004. Applications of modelling to optimise ultra high temperature milk heat exchangers with respect to fouling. Food Control 15, 117–130.

Guérin, R., Ronse, G., Bouvier, L., Debreyne, P., Delaplace, G., 2007. Structure and rate of growth of whey protein deposit from in situ electrical conductivity during fouling in a plate heat exchanger. Chem. Eng. Sci. 62, 1948–1957.

Hagsten, C., Innings, F., Trägårdh, C., Hamberg, L., Paulsson, M., Nylander, T., 2019. Removal of UHT dairy fouling – an efficient cleaning process by optimizing the rate controlling alkaline cleaning step. Food Bioprod. Process. 113, 101–107.

Jeyarajah, S., Allen, J.C., 1994. Calcium binding and salt-induced structural changes of native and preheated.beta.-lactoglobulin. J. Agric. Food Chem. 42, 80–85.

Jun, S., Puri, V.M., 2005. 3D milk-fouling model of plate heat exchangers using computational fluid dynamics. Int. J. Dairy Technol. 58, 214–224.

Jun, S., Puri, V.M., 2006. A 2D dynamic model for fouling performance of plate heat exchangers. J. Food Eng. 75, 364–374.

Jun, S., M. Puri, V., Roberts, R, F., 2004. A dynamic 2D model for thermal performance of plate heat exchangers. Trans. ASAE 47, 213–222.

Khaldi, M., Blanpain-Avet, P., Guérin, R., Ronse, G., Bouvier, L., André, C., Bornaz, S., Croguennec, T., Jeantet, R., Delaplace, G., 2015. Effect of calcium content and flow regime on whey protein fouling and cleaning in a plate heat exchanger. J. Food Eng. 147, 68–78.

Khaldi, M., Croguennec, T., André, C., Ronse, G., Jimenez, M., Bellayer, S., Blanpain-Avet, P., Bouvier, L., Six, T., Bornaz, S., Jeantet, R., Delaplace, G., 2018. Effect of the calcium/protein molar ratio on β-lactoglobulin denaturation kinetics and fouling phenomena. Int. Dairy J. 78, 1–10.

Kroslak, M., Sefcik, J., Morbidelli, M., 2007. Effects of temperature, pH, and salt concentration on β-lactoglobulin deposition kinetics studied by optical waveguide lightmode spectroscopy. Biomacromolecules 8, 963–970.

Liu, W., Wilson, D.I., Chen, X.D., Mercadé-Prieto, R., 2018. Quantification of the local protein content in hydrogels undergoing swelling and dissolution at alkaline ph using fluorescence microscopy. Food Bioprocess Technology 11, 572–584.

Liu, W., Chen, X.D., Jeantet, R., André, C., Bellayer, S., Delaplace, G., 2021. Effect of casein/whey ratio on the thermal denaturation of whey proteins and subsequent fouling in a plate heat exchanger. J. Food Eng. 289, 110175.
Liu, W., Feng, Y., Delaplace, G., André, C., Chen, X.D., 2022. Effect of calcium on the reversible and irreversible thermal denaturation pathway of β-lactoglobulin. Food Hydrocoll. 133, 107943.
Liu, W.J., Chen, X.D., Mercadé-Prieto, R., 2017. Spatial quantification of hydrogels swelling using wide-field fluorescence microscopy. Chem. Eng. Sci. 158, 349–358.
López Arbeloa, T., López Arbeloa, F., López Arbeloa, I., 1999. Environmental effects on the photophysics of pyrromethene 556. Phys. Chem. Chem. Phys. 1, 791–795.
Mahdi, Y., Mouheb, A., Oufer, L., 2009. A dynamic model for milk fouling in a plate heat exchanger. Appl. Math. Model. 33, 648–662.
Nema, P.K., Datta, A.K., 2006. Improved milk fouling simulation in a helical triple tube heat exchanger. Int. J. Heat. Mass Transf. 49, 3360–3370.
Oldfield, D.J., Singh, H., Taylor, M.W., Pearce, K.N., 1998. Kinetics of denaturation and aggregation of whey proteins in skim milk heated in an ultra-high temperature (UHT) pilot plant. Int. Dairy J. 8, 311–318.
Pan, F., Chen, X.D., Mercadé-Prieto, R., Xiao, J., 2019. Numerical simulation of milk fouling: taking fouling layer domain and localized surface reaction kinetics into account. Chem. Eng. Sci. 197, 306–316.
Paviolo, C., Clayton, A.H.A., McArthur, S.L., Stoddart, P.R., 2013. Temperature measurement in the microscopic regime: a comparison between fluorescence lifetime- and intensity-based methods. J. Microsc. 250, 179–188.
Petit, J., Herbig, A.L., Moreau, A., Delaplace, G., 2011. Influence of calcium on β-lactoglobulin denaturation kinetics: implications in unfolding and aggregation mechanisms. J. Dairy Sci. 94, 5794–5810.
Petit, J., Six, T., Moreau, A., Ronse, G., Delaplace, G., 2013. β-lactoglobulin denaturation, aggregation, and fouling in a plate heat exchanger: pilot-scale experiments and dimensional analysis. Chem. Eng. Sci. 101, 432–450.
de sa, Peres, Peixoto Junior, P., Trivelli, X., Andre, C., Moreau, A., Delaplace, G., 2019. Formation of beta-lactoglobulin aggregates from quite, unfolded conformations upon heat aαctivation. Langmuir: ACS J. Surf. Colloids 35, 446–452.
Sadeghinezhad, E., Kazi, S.N., Dahari, M., Safaei, M.R., Sadri, R., Badarudin, A., 2015. A comprehensive review of milk fouling on heated surfaces. Crit. Rev. Food Sci. Nutr. 55, 1724–1743.
Sahoo, P.K., Ansari, I.A., Datta, A.K., 2005. Milk fouling simulation in helical triple tube heat exchanger. J. Food Eng. 69, 235–244.
Santos, O., Nylander, T., Schillén, K., Paulsson, M., Trägårdh, C., 2006. Effect of surface and bulk solution properties on the adsorption of whey protein onto steel surfaces at high temperature. J. Food Eng. 73, 174–189.
Sawyer, W.H., 1969. Complex between beta-lactoglobulin and kappa-casein. A review. J. Dairy Sci. 52, 1347–1355.
Shimada, K., Cheftel, J.C., 2002. Sulfhydryl group/disulfide bond interchange reactions during heat-induced gelation of whey protein isolate. J. Agric. Food Chem. 37, 161–168.
Simons, J.-W.F.A., Kosters, H.A., Visschers, R.W., de Jongh, H.H.J., 2002. Role of calcium as trigger in thermal β-lactoglobulin aggregation. Arch. Biochem. Biophys. 406, 143–152.
Smart, P.L., Laidlaw, I.M.S., 1977. An evaluation of some fluorescent dyes for water tracing. Water Resour. Res. 13, 15–33.
Vasbinder, A.J., de Kruif, C.G., 2003. Casein–whey protein interactions in heated milk: the influence of pH. Int. Dairy J. 13, 669–677.
Verheul, M., Roefs, S.P.F.M., de Kruif, K.G., 1998. Kinetics of heat-induced aggregation of β-lactoglobulin. J. Agric. Food Chem. 46, 896–903.
Wijayanti, H.B., Bansal, N., Deeth, H.C., 2014. Stability of whey proteins during thermal processing: a review. Compr. Rev. Food Sci. Food Saf. 13, 1235–1251.
Yang, W., Li, D., Chen, X.D., Mercadé-Prieto, R., 2018. Effect of calcium on the fouling of whey protein isolate on stainless steel using QCM-D. Chem. Eng. Sci. 177, 501–508.